Materialia 2 (2018) 73–81

Contents lists available at ScienceDirect

Materialia

journal homepage: www.elsevier.com/locate/mtla

Full Length Article

Evolution of local lattice distortion under irradiation in medium- and high-entropy alloys☆

Y. Tong[a], G. Velisa[a], S. Zhao[a], W. Guo[b], T. Yang[c], K. Jin[a], C. Lu[c], H. Bei[a], J.Y.P. Ko[d], D.C. Pagan[d], Y. Zhang[a,e], L. Wang[c], F.X. Zhang[a,*]

[a] Division of Materials Science and Technology, Oak Ridge National Laboratory, Oak Ridge, TN 37831, USA
[b] Center for Nanophase Materials Sciences, Oak Ridge National Laboratory, Oak Ridge, TN 37831, USA
[c] Department of Nuclear Engineering and Radiological Sciences, University of Michigan, Ann Arbor, MI 48109, USA
[d] Cornell High Energy Synchrotron Source, Cornell University, Ithaca, NY 14850, USA
[e] Department of Materials Science and Engineering, The University of Tennessee, Knoxville, TN 37996, USA

ARTICLE INFO

Keywords:
High-entropy alloys
Lattice distortion
Pair distribution function
Ion irradiation
Density functional theory calculation

ABSTRACT

A major challenge for future nuclear reactors is to design nuclear materials that can sustain extremely prolonged radiation damage. Local lattice distortion, considered as a core effect of high-entropy alloys (HEAs), can suppress the growth of radiation defects to control radiation performance. However, local lattice distortion in HEAs is rarely quantitatively measured. Here we employed total scattering technique to study the local structure of the face-centered cubic (fcc) equiatomic FeCoNiCr MEA, and FeCoNiCrMn and FeCoNiCrPd HEAs before and after ion irradiation. Their local lattice distortions were quantitatively evaluated based on the difference of lattice constant between the local structure and the average structure. We revealed that the mean local lattice distortion in the pristine samples varies in the following order: FeCoNiCr < FeCoNiCrMn < FeCoNiCrPd. Density functional theory (DFT) calculations further unveiled that the fluctuation of local distortions in FeCoNiCr and FeCoNiCrMn is less than 5%, whereas the highest bond-length fluctuation in FeCoNiCrPd can approach to 8%. Under irradiation the mean local lattice distortion in FeCoNiCr and FeCoNiCrMn evolves differently from FeCoNiCrPd by showing a relaxation behavior at low dose. And the impact of local lattice distortion on dislocation loops after a prolonged ion-irradiation was investigated by transmission electron microscope (TEM) and the underlying mechanism was discussed.

1. Introduction

HEAs owe their name to the large contribution of configurational entropy to the Gibbs free energy by mixing five or more elements to favor a single solid solution phase [1,2]. As single-phase concentrated solid-solution alloys (SP-CSAs), it is conceivable that compositional complexity can bring HEAs a relatively large fluctuation in the local chemical and physical environments because of differences in enthalpy and atomic size mismatch among each atomic pair, which may offer opportunities to find new properties.

The compositional complexity that results from alloying multiple d transition metals in the fcc SP-CSAs has produced remarkable properties for extreme environment applications [3–8], in particular damage resistance in high-radiation environments. For example, the adjustment of local chemical environment in SP-CSAs by mixing different elements or varying concentration dramatically increases their electrical resistivity and decreases their thermal conductivity [6,9], potentially assisting recombination of irradiation-induced point defects due to a prolonged thermal spike under irradiation [6]. Recently, FeCoNiCrMn (denoted by Mn-HEA hereafter) and FeCoNiCrPd (denoted by Pd-HEA hereafter) HEAs were reported to have the lowest electrical conductivity and thermal conductivity among the studied CSAs, including NiFe, NiCo, NiCoCr, NiCoFe and NiCoFeCr [9]. Consistently, Mn-HEA was found to exhibit the minimum swelling (< 0.2%) among other CSAs after Ni^{2+} ion irradiation at 773 K [7,10]. On the other hand, large lattice distortions can retard dislocation movement to suppress the growth of

* Corresponding author.
E-mail address: zhangf@ornl.gov (F.X. Zhang).

https://doi.org/10.1016/j.mtla.2018.06.008
Received 15 June 2018; Accepted 20 June 2018
Available online 27 June 2018

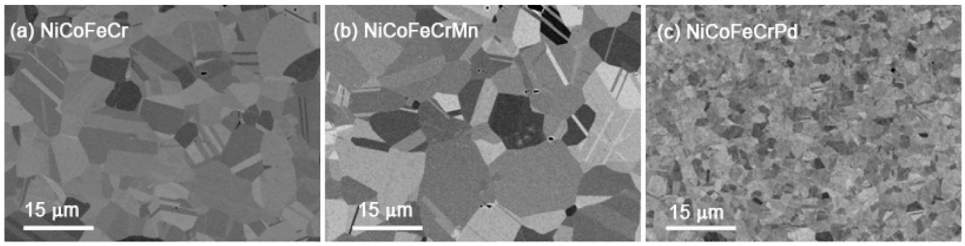

Fig. 1. Microstructure of the prepared samples. Backscattered electron images of (a) FeCoNiCr, (b)Mn-HEA, and (c) Pd-HEA.

damage structures [5,11]. It is also worth mentioning that undersized or oversized solute can suppress radiation-induced segregation at grain boundaries and void swelling by trapping point defects demonstrated by austenitic or ferritic steels [12–17]. HEAs are expected to minimize damage evolution because their compositional complexity produces an intrinsically maximized lattice distortion.

However, the core effect of severe lattice distortion in HEAs remains under debate. Several experiments have been conducted to evaluate the lattice distortion in medium-entropy alloys [18,19] (MEAs, alloys with three or four elements in equimolar or near equimolar fraction) and the Mn-HEA [20]. Strong local lattice distortion has been claimed in the loosely-packed body-centered cubic (bcc) ZrNbHf and NbMoTaW MEAs based on qualitative observations [18,19]. Meanwhile, first-principle calculation results suggest that the fluctuation of atomic displacements in the bcc ZrNbHf and HfNbTiZr MEAs and HfNbTaTiZr HEA can approach to ~10% [21]. However, pair distribution function (PDF) measurements show no evidence of strong local lattice distortion in the closely-packed fcc $Ni_{37.5}Co_{37.5}Cr_{25}$ MEA and Mn-HEA [20]. A quantitative analysis based on extended x-ray absorption fine structure measurement demonstrates that the mean local lattice distortion in the Mn-HEA is extremely small (~0.1%), but first-principle calculations reveal that its bond distances can fluctuate to 5% [22]. More experimental and simulation studies are strongly needed to both quantitatively evaluate local distortions in newly-developed HEAs and to link the local lattice distortion effect with their properties.

In the present study, we quantitatively characterized the mean local lattice distortion and its evolution under ion irradiation in the FeCoNiCr, Mn-HEA and Pd-HEA. The most-studied Mn-HEA [3,20,23–25] and its base alloy, FeCoNiCr, were investigated for comparison. Meanwhile, DFT calculations were conducted to study the fluctuation of local distortions. The impact of local lattice distortion on the growth of radiation defects were investigated by transmission electron microscope (TEM) and the underlying mechanism was discussed.

2. Experimental

2.1. Material preparation

Elemental Ni, Co, Fe, Cr, Mn and Pd (> 99% pure) were mixed into equi-atomic NiCoFeCr, NiCoFeCrMn, and NiCoFeCrPd by arc melting. The arc-melted buttons were flipped and re-melted at least five times to improve homogeneity and then drop cast into a copper mold to form ingots with dimensions of $12.7 \times 12.7 \times 70$ mm^3. The ingots were homogenized for 24 h at 1473 K, and then rolled at room temperature to a final thickness of ~1.8 mm. The rolled specimens were annealed at 1073 K for 1 h. After above processing, all alloys show equiaxed grain microstructure with an averaged grain size of approximately 6 μm, 8 μm and 2 μm for FeCoNiCr, FeCoNiCrMn and FeCoNiCrPd, respectively (Fig. 1).

2.2. Ion irradiation

Stripe samples with a thickness of 150 μm were irradiated with multiple energies of Ni ions (the order is 16 MeV Ni^{5+}, 8 MeV Ni^{3+}, 4 MeV Ni^{1+} and then 2 MeV Ni^{1+}) to various fluences (0.1 dpa, 0.3 dpa, and 1dpa; see Table 1 for details) at room temperature for total scattering study. The details about multiple-energy irradiation can be found in refs [26,27]. Also, specimens after 3 MeV Ni^{2+} ion irradiation up to 55 ± 5 dpa at 693 K were used for the TEM microstructural characterization. During the ion irradiation, a raster ion beam was used to ensure a homogeneous irradiation. All the irradiation experiments were carried out in the Ion Beam Materials Laboratory at the University of Tennessee. Predictions of local dose in samples were calculated by the Stopping and Range of Ions in Matter 08 code (SRIM 08) in Kinchin-Pease option simulation mode [28] assuming a displacement threshold energy of 40 eV for all elements. The multiple-energy irradiation generated a region of approximately uniform damage to a depth of about 3500 nm based on SRIM damage profile calculation.

Table 1
Irradiation conditions (ion energy and species, dose at damage peak position and fluence).

	0.1 dpa	0.3 dpa	1 dpa
16 MeV Ni^{5+}	1.5 /nm^2	5 /nm^2	15 /nm^2
8 MeV Ni^{3+}	0.49 /nm^2	1.63 /nm^2	4.9 /nm^2
4 MeV Ni^{1+}	0.49 /nm^2	1.63 /nm^2	4.9 /nm^2
2 MeV Ni^{1+}	0.35 /nm^2	1.16 /nm^2	3.5 /nm^2

2.3. Characterization

The total scattering measurement was carried out at room temperature at F2 station of CHESS with an X-ray energy of 61 keV ($\lambda = 0.2022$ Å) and 28-ID beamline of NSLS II with an X-ray energy 67 keV ($\lambda = 0.185$ Å). The beam size was 500×500 μm^2. A two-dimensional stationary detector with 200×200 μm^2 pixel size was placed ~20 cm behind the sample to collect data. Calibration was performed using CeO_2 NIST powder standard. Fit2D software [29] was used to correct for a beam polarization and a dark current. PDFgetX3 [30] was used to obtain real-space PDF by a Fourier transformation of the measured and then normalized reciprocal-space structure function in a Q range of 30 $Å^{-1}$. By using PDFGUI software [31] the measured PDFs were refined with structure models.

Cross-sectional TEM foils were prepared by focused ion beam lift-out techniques on a FEI Helios Nanolab Dualbeam workstation in the Michigan Center for Materials Characterization at the University of Michigan. Bright-field TEM imaging of dislocation loops were taken in a two-beam condition ($g = [200]$) using JEOL 3011. To minimize the artificial effects from surface sinks and injected interstitials [32], the region of 700 ± 100 nm with a damage dose of 50 ± 5 dpa calculated by SRIM 08 [28] was chosen for the statistical study of loop distribution.

For the atom probe tomography (APT) observation, an FEI Nova 200 dual-beam focused-ion-beam instrument was utilized to perform lift-outs and annular milling to fabricate the needle shaped APT specimens. The APT analysis was conducted with a local electrode atom probe (CAMECA LEAP 4000x HR) in a laser mode with a 50 pJ pulse energy at

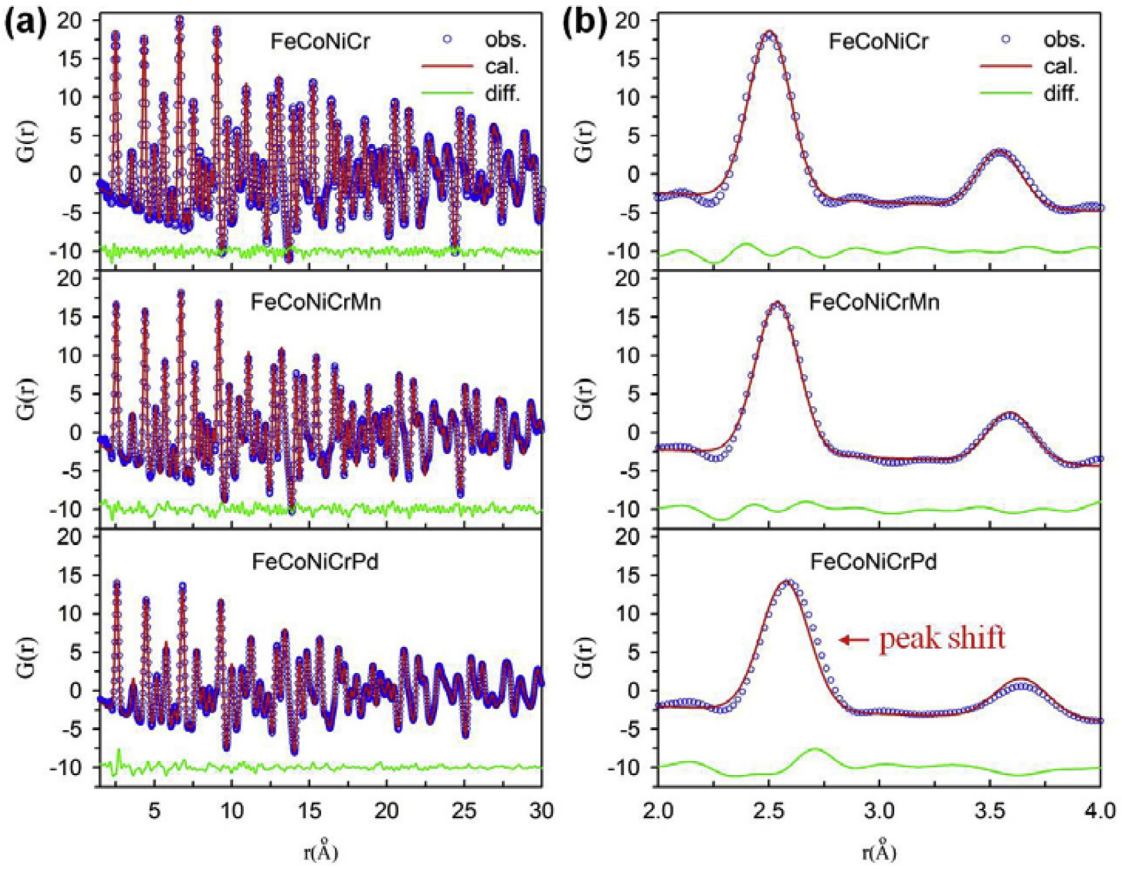

Fig. 2. (a) A comparison between the observed X-ray PDF and the PDF calculated from an ideal fcc structure with identical occupancies of different atomic species. (b) An enlarged view of the local structure in (a). The green line at the bottom of each figure shows the difference in PDF.

30 K and a detection rate of 0.005 atoms per pulse. The data sets were reconstructed and analyzed using the IVAS 3.6.12 software.

2.4. Density functional theory calculation

DFT calculations were performed using the Vienna *ab initio* simulation package (VASP) [33]. The exchange and correlation interactions were described by a gradient corrected functional in the Perdew-Burke-Ernzerhof (PBE) form [34]. Standard projector-augmented-wave (PAW) pseudopotentials distributed with VASP were used to treat electron-ion interactions [35]. The energy cutoff for the plane-wave basis set was set to be 350 eV. The energy and force convergence criterion were set to be 10^{-4} eV and 0.01 eV/Å. All calculations were performed with spin-polarization to account for the magnetic properties of considered alloys. The chemical disorder of alloys was modeled by special quasi-random structures (SQS) [36] that were constructed using a simulated annealing Monte-Carlo algorithm. The supercells (contain 144 atoms) were oriented along the $[\bar{1}10]$, [112] and $[\bar{1}\bar{1}1]$ directions, as used in our previous study [37]. For each composition, three SQS were constructed to verify the reliability of the DFT calculations. Both cell parameters and internal coordinates were fully optimized in the calculations.

3. Results

3.1. Local lattice distortion in pristine samples

Local lattice distortion produces diffuse scattering embedded in the background underneath Bragg peaks, so PDF as a result of the Fourier transformation of both Bragg peaks and diffuse scattering (i.e., total scattering) looks beyond the average structure to provide local structure information in terms of inter-atomic distance [38]. Fig. 2(a) compares the observed PDFs with the ones calculated from an ideal fcc structure with random arrangements of different elements on the same crystallographic sites, and their difference shows some distinct features for these alloys. The PDF difference curve for the FeCoNiCr MEA has no visible r dependence, and random noise over the whole r range indicates a good fitting (the goodness-of-fit parameter, R_w, is ~0.073) with the ideal random structure model. Although the PDF difference curve for Mn-HEA shows a similar behavior as FeCoNiCr, a subtle difference exists at the short r range. An enlarged view of its local structure in Fig. 2(b) shows that the calculated PDF slightly deviates from the measured data at the right shoulder of the first PDF peak. For Pd-HEA the difference curve exhibits an apparent r-dependent behavior, especially a large deviation in the first atomic shell, indicating a deviation of local structure at short r range from the average structure at high r range. Fig. 2(b) enlarges the detail of the local structure deviation in Pd-HEA. The measured first PDF peak shifts to the high r direction with respect to the modeled peak, revealing a larger average bond distance among the nearest atomic neighbors than expected in Pd-HEA.

A commonly-used method to qualitatively analyze local lattice distortion in materials is the measurement of the PDF peak width or the attenuation of the PDF peak intensity since they contain contributions from both thermal and static displacements. Fig. 2(a) clearly shows that the addition of Pd into FeCoNiCr MEA strongly damps the envelop of PDF peaks while dramatically broadens the PDF peaks, and Mn has a relatively small effect (consistent with a recent neutron PDF measurement [20]). The Debye-Waller (DW) factor extracted from the PDF fitting ($\sigma^2_{\text{FeCoNiCr}} \sim 0.0065\ \text{Å}^2$, $\sigma^2_{\text{Mn-HEA}} \sim 0.0066\ \text{Å}^2$, and $\sigma^2_{\text{Pd-HEA}} \sim 0.0098\ \text{Å}^2$) reveals that the $\sigma_{\text{Pd-HEA}}$ of Pd-HEA is larger by ~0.018 Å than those of FeCoNiCr and Mn-HEA. FeCoNiCr

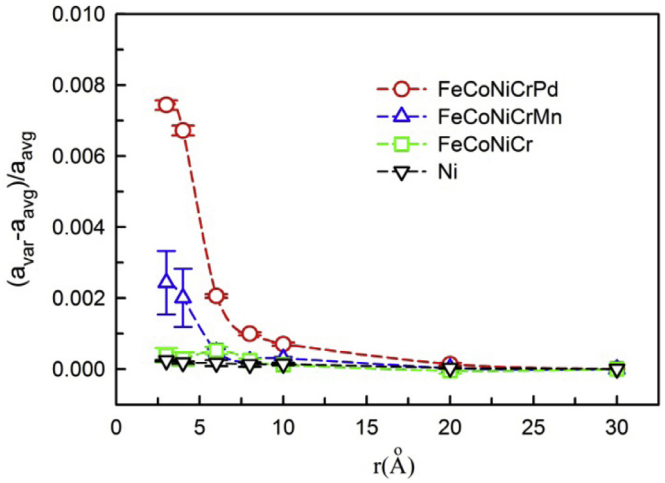

Fig. 3. Dependence of lattice constant on variation of fitting range. The r range in all PDF fittings starts from 1.5 Å but ends at different r value. a_{var} denotes the r dependent lattice constant and a_{avg} is the lattice constant of the average structure obtained from a full spectrum fitting. Standard Ni powder sample was used as a benchmark for non-distorted fcc structure.

and Mn-HEA have a similar magnitude of DW factor, but thermal displacement in Mn-HEA can be higher than the FeCoNiCr case because of the low melting temperature of Mn-HEA (T_m = 1553 K [39]) compared with FeCoNiCr (T_m = 1695 K [39]). The melting temperature of Pd-HEA (T_m = 1560 K, which was measured by a NETZSCH 404 C differential scanning calorimeter; details about the measurement can be found in ref. [39]) is comparable with the one of Mn-HEA and heavy element commonly leads to a small thermal displacement, so it is highly possible that the static displacement provides a major contribution to the increase of the magnitude of the DW factor and the broadening of the PDF peaks in Pd-HEA. However, the difficulty associated with this type of analysis is the separation of different displacement components [20].

Instead, the local distortion can be quantitatively analyzed by considering the difference in lattice constant extracted from varying r-range refinement, denoted by a_{var}. Here, the refinement is based on the ideal, non-distorted fcc structure. The major advantage of this quantitative method is the separation of static and thermal displacements since the equilibrium position of atoms in a given crystal structure is only determined by the position of the PDF peak. For the varying r-range refinement we fixed the r_{min} to 1.5 Å but varied r_{max} to gradually increase the weight of average structure. The lattice constant obtained from a full spectrum fitting can be considered as the lattice constant of the average structure (denoted as a_{avg} hereafter). An r_{min} of 1.5 Å was chosen to exclude the large noise at the low r range due to Fourier transformation of the structure function with a finite Q range [38]. The normalized variation of a_{var} with reference to a_{avg} is defined as lattice distortion, $\varepsilon_{var} = (a_{var} - a_{avg})/a_{avg}$. Fig. 3 shows the r dependence of ε_{var}. Standard Ni powder sample was also measured and analyzed to benchmark the reliability of the local lattice distortion in HEAs because pure Ni has no size mismatch and thus zero lattice distortion. Compared with the pure Ni, the FeCoNiCr MEA has a negligible local lattice distortion with the variation of fitting range. However, for Mn- and Pd-HEAs positive lattice distortion appears at short range, revealing that the local lattice is under expansion, and this local lattice distortion is strongly localized by a quick decay above the second atomic shell (~4 Å). In the Pd-HEA with a bond length of 2.62 Å, a 0.74% local lattice distortion in the 1st atomic shell should yield a static displacement of 0.019 Å, which contributes ~20% to its DW factor, σ_{Pd-HEA}. Also, we calculated that the static displacements in the FeCoNiCr and Mn-HEA share ~1.2% and ~7.4% of the $\sigma_{FeCoNiCr}$ and σ_{Mn-HEA}, respectively.

Additionally, Fig. 4 was shown to emphasize the large local structure deviation from the average structure in the Pd-HEA when compared with the pure Ni. In the upper panels of Fig. 4, the measured PDFs were fitted over the whole r range to obtain the a_{avg}, while in the lower panels the first PDF peak was fitted to obtain the a_{1st} and then the fitting was extended to the whole r range but with lattice constant parameter fixed as a_{1st}. The Ni sample has an excellent fitting, $R_w \sim 0.02$, for both refinement cases, and the slight difference between a_{1st} and a_{avg} is within the error range. But Pd-HEA has poor fitting, $R_w \sim 0.3$, when the lattice parameter was fixed as a_{1st}, where the calculated PDF is completely out of phase with the measured one at high r range though the first PDF peak is well fitted.

3.2. Local lattice distortion in irradiated samples

The size mismatch effect is often considered as a static factor to benefit the radiation performance of nuclear materials, though their local structure and crystal structure can be significantly damaged after irradiation. Here, we show for the first time a dynamic evolution of the atomic size misfit in CSAs under irradiation. Irradiation with multiple energies of Ni ions to various fluences were conducted to produce a deep and uniform damage region (3.5 μm) [27]. The purpose of generating deep damage region is to enhance a signal-to-noise ratio in PDF measurements. Fig. 5(a) shows the variation of a_{avg} with the radiation dose for the three studied alloys. We find that with increasing radiation dose the average lattice constant expands quickly at first and then reaches to a steady state, in agreement with the conventional X-ray diffraction measurements [40–42]. Molecule dynamics simulations [42] revealed that point defects and small clusters produce volume strain while their growth into large defect clusters, e.g. dislocation loop, leads to a relaxation of the volume strain. It is conceivable that the steady lattice expansion is closely related to a balancing competition of the production rate of small radiation defects with their growth rate.

Fig. 5(b) plots the dose dependence of the local lattice distortion in the 1st atomic shell, $\varepsilon_{1st} = (a_{1st} - a_{avg})/a_{avg}$. We can see that the ε_{1st} behaves abnormally compared with the expansion of a_{avg} in Fig. 5(a). The local distortion, ε_{1st}, in FeCoNiCr and Mn-HEA shows a relaxation phenomenon at the early stage of ion irradiation and then increases at the later steady state, whereas the local distortion in Pd-HEA monotonically increases with the dose. For FeCoNiCr and Mn-HEA the relaxed local distortion should be attributed to the surge of the lattice expansion at the low dose stage since the lattice expansion at 1 dpa for these two alloys is comparable with the initial local distortion in the pristine samples. In contrast, the initial local lattice distortion in Pd-HEA is large enough (0.74%) to compensate the relatively small lattice expansion (0.32% at 1 dpa), avoiding the local distortion relaxation occurred in other two CSAs. Moreover, the buildup of local lattice distortion in Pd-HEA may further improve its radiation tolerance by increasing the defect pinning capability. Since a stable defect pinning is critical for a continuous recombination of radiation-induced defects in nuclear materials during their service time, the sharp decrease of the local lattice distortion in FeCoNiCr and Mn-HEA starting at a very low dose should be prevented. The dynamic evolution of local lattice distortion under ion irradiation suggests that a critical value of atomic size misfit (larger than average lattice expansion) is required for an alloy to prohibit a relaxation behavior. Therefore, the size effect cannot be regarded as a static factor when samples are under irradiation.

Due to a strong local lattice distortion, Pd-HEA is expected to have an excellent capability to pin dislocations and thus delay their growth. To verify this hypothesis, Mn- and Pd-HEAs were irradiated with 3 MeV Ni^{2+} ions up to 55 ± 5 dpa at the region of 700 ± 100 nm from the sample surface at 693 K. Here, the chosen irradiation condition is based on the fact that under such high dose and temperature dislocation loop growth is mainly controlled by interactions among them [43]. After such a prolonged irradiation at elevated temperature, dislocation loops in these two irradiated HEAs were examined by TEM, as shown in

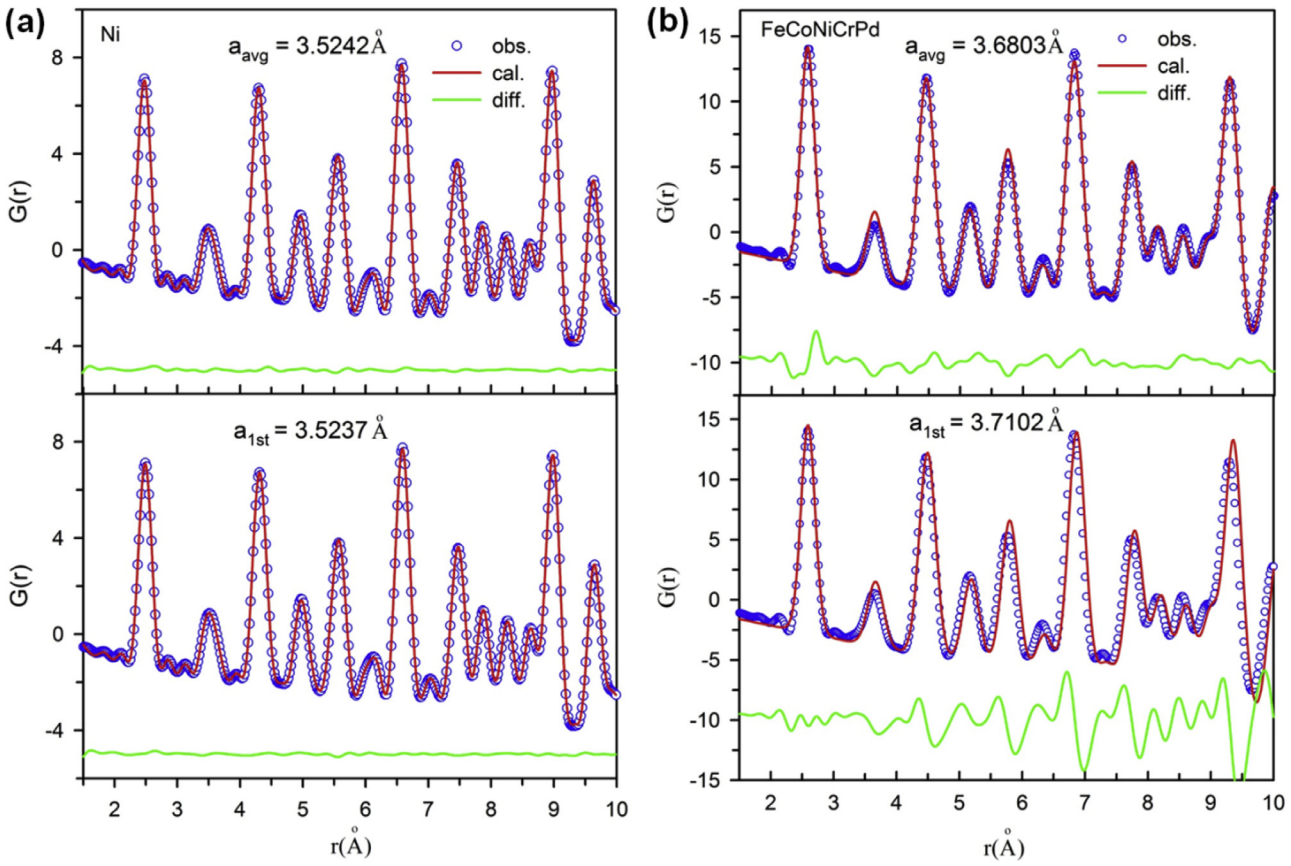

Fig. 4. Deviation of local lattice constant, a_{1st}, from average lattice constant, a_{avg} for Ni powder sample (a) and FeCoNiCrPd HEA (b). In the upper panels, the measured PDFs were fitted over the whole r range, whereas in the lower panels, the first PDF peak was fitted to obtain the a_{1st} and then the fitting was extended to the whole r range but with lattice constant parameter fixed as a_{1st}. For Ni sample, the difference between a_{1st} and a_{avg} is comparable with error, but FeCoNiCrPd HEA shows a large difference.

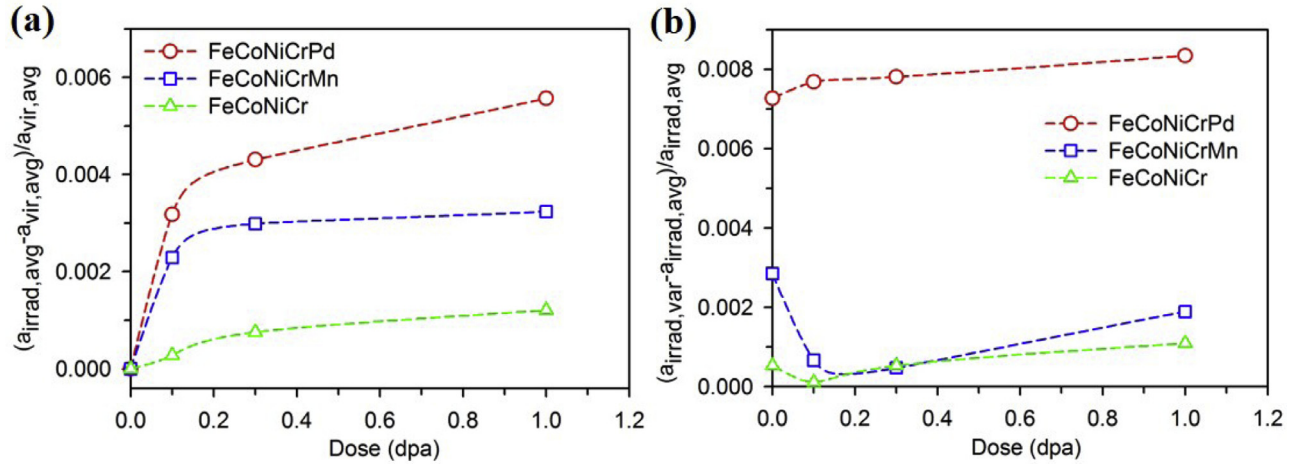

Fig. 5. Ion irradiation effect on the lattice constant of the average structure (a) and the lattice distortion in the 1st atomic shell (b). Here, $a_{irrad,\ var}$ was extracted from the PDF fitting in the r range from 1.5 Å to 3 Å, covering only the 1st atomic shell.

Fig. 6. Compared to Mn-HEA, Pd-HEA has a high density of dislocation loops (Pd-HEA: $(19.6 \pm 2) \times 10^{21}$ m^{-3}, and Mn-HEA: $(5.83 \pm 0.6) \times 10^{21}$ m^{-3}) but with a very small average size (Pd-HEA: 4.7 ± 1 nm, and Mn-HEA: 15.9 ± 1 nm). Additionally, previous studies showed that the average dislocation loop size in FeCoNiCr is twice larger than the one in Mn-HEA under 3 MeV Ni^{2+} ions irradiation to 38 ± 5 dpa at 773 K [5,11]. Large local lattice distortion in Pd-HEA can both directly and indirectly influence the growth of dislocation loops. Considering the direct pinning effect, the dislocation-local distortion interaction in Pd-HEA could be 6 times higher than the Mn-HEA case. Here, the interaction is roughly estimated based on the conventional Fleischer-type relationship between solution strengthening ($\Delta\sigma_s$) and size mismatch (ε_s) [44], $\Delta\sigma_s \propto \varepsilon_s^{3/2}$. Notice that modulus mismatch also contributes to the solution strengthening. The shear moduli are 84 GPa, 80 GPa and 86 GPa for the FeCoNiCr MEA, Mn-HEA and Pd-HEA, respectively [39]. Due to the small difference among their shear moduli, the solution strength-

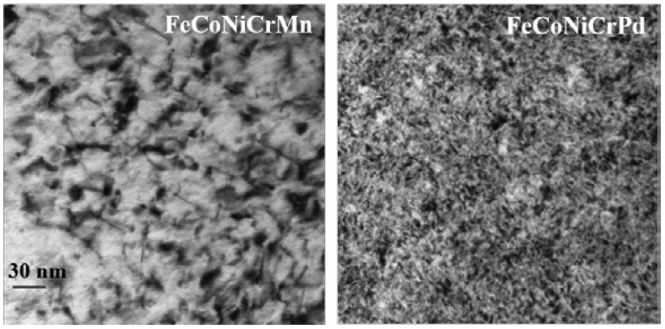

Fig. 6. TEM imaging of radiation defects. Dislocation loops in two-beam condition bright-field images of Mn- and Pd HEAs irradiated to 50 ± 5 dpa at 700 ± 100 nm from the surface at 693 K.

ening from the modulus mismatch (ε_G) contribution is comparable for Mn-HEA (ε_G = 0.02) and Pd-HEA (ε_G = 0.05). Therefore, local lattice distortion is the dominant factor for the slow growth of dislocation loops in the irradiated Pd-HEA. On the other hand, large local lattice distortion reduces the thermal conductivity of Pd-HEA by strong scattering of free electrons, which can prolong the thermal spike lifetime leading to an effective recombination of interstitials and vacancies at the early defect evolution stage [6]. Furthermore, from the perspective of energy minimization oversized Pd atoms prefer trapping vacancies to release lattice strain, potentially increasing the probability of recombining vacancies with nearby interstitial loops. Note that vacancy diffusion can be accelerated by large atoms [45–48] and a balance between vacancy diffusion and dislocation pinning is needed to optimize the recombination probability. Predicatively, the defect recombination in Pd-HEA can be further improved by optimizing the Pd concentration.

Table 2
A comparison of local lattice distortion between predications and experimental results.

Composition	ε_{1st} (%)	δ [52]	ε_{RMS} (%) [52]	σ (%)
FeCoNiCr	0.04 ± 0.02	0.3	0.39	1.11
FeCoNiCrMn	0.24 ± 0.09	3.27	3.25	1.09
FeCoNiCrPd	0.74 ± 0.01	4.46	4.46	3.52

1st denotes the 1st atomic shell.

4. Discussion

Several parameters based on hard sphere packing have been proposed to estimate the size mismatch effect in HEAs [49–51]. Zhang et al. [49] estimated the size mismatch effect in HEAs by a parameter,

$$\delta\% = \sqrt{\sum_{i=1}^{N} c_i \left(1 - r_i / \sum_{j=1}^{N} c_j r_j\right)^2}$$

, where N, $c_{i,j}$ and $r_{i,j}$ are the total number of the constituent elements, the atomic fraction and atomic radius of the ith or jth element, respectively. Additionally, Ye et al. [50,52] calculated the fluctuation of local residual strain, ε_{RMS}, in HEAs. In Table 2, a comparison is made between our experimental results and their calculations. The values of δ and ε_{RMS} are very close, but these two parameters are one order of magnitude larger than the ε_{1st} we measured. Still, a general agreement that local lattice distortion increases with increasing atomic size mismatch can be reached among the calculations and our measurement. The reason for the large difference between ε_{1st} and the calculated parameters is revealed below.

DFT calculations have revealed that the fluctuation of the atomic displacement in HEAs can be a few percent of bond distance [21,22,53,54]. To find the fluctuation of the atomic displacement in FeCoNiCr, Mn-HEA and Pd-HEA, distorted structure models were created at first by intro-

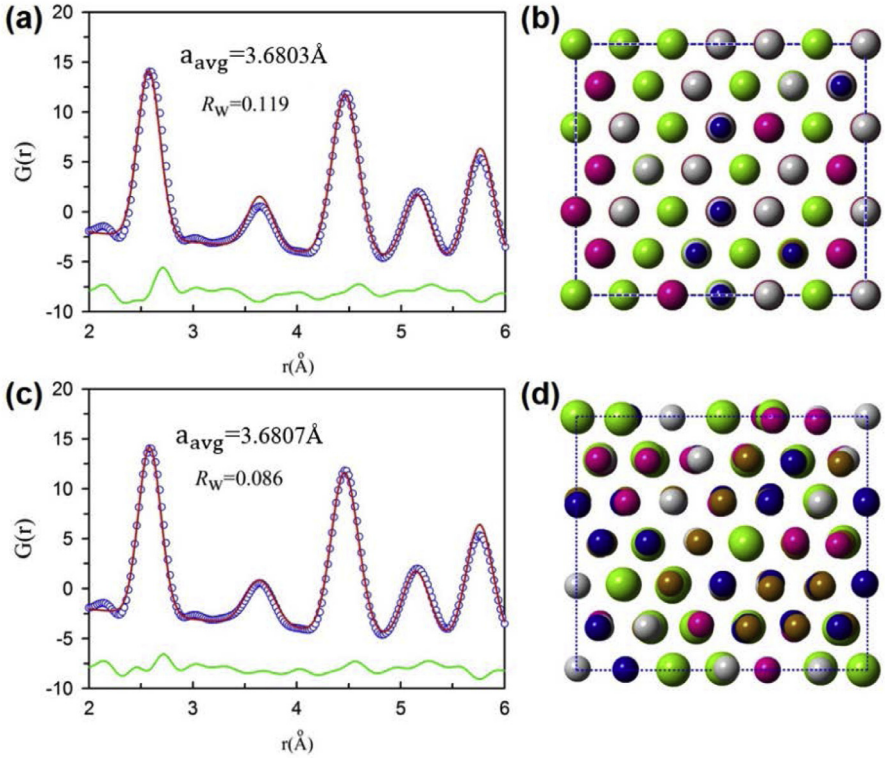

Fig. 7. (a) PDF fitting with the ideal, non-distorted FCC structure in (b). (c) PDF fitting with the relaxed and distorted FCC structure in (d) obtained from DFT simulation. (b) and (d) are along the view of [111] direction. Co atoms are in blue, Cr in magenta, Fe in brown, Ni in gray and Pd in green.

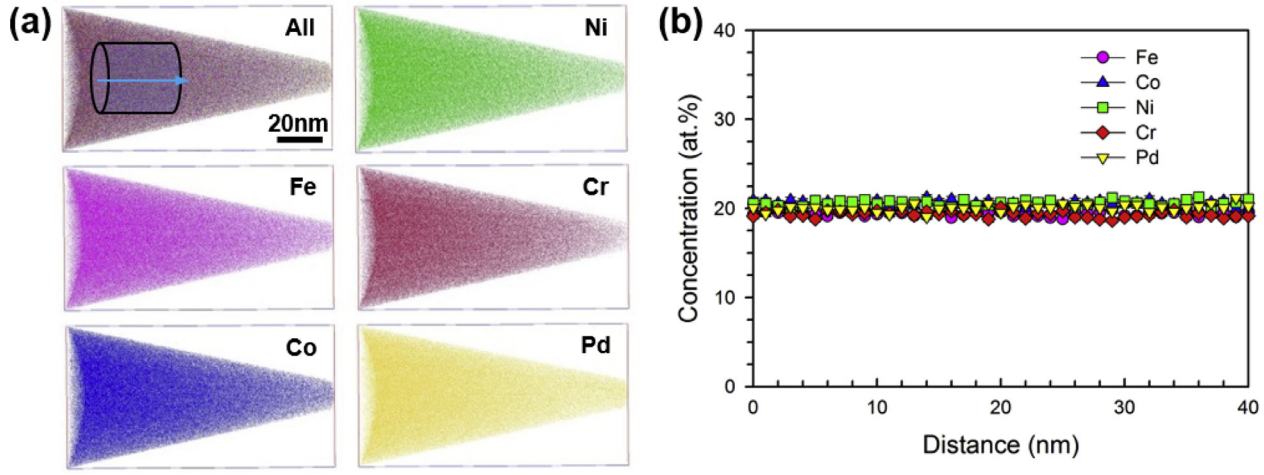

Fig. 8. Chemical homogeneity in Pd-HEA. (a) Atom maps showing uniform distribution of each component in Pd-HEA. (b) Concentration profiles of all elements along the cylinder indicated in (a).

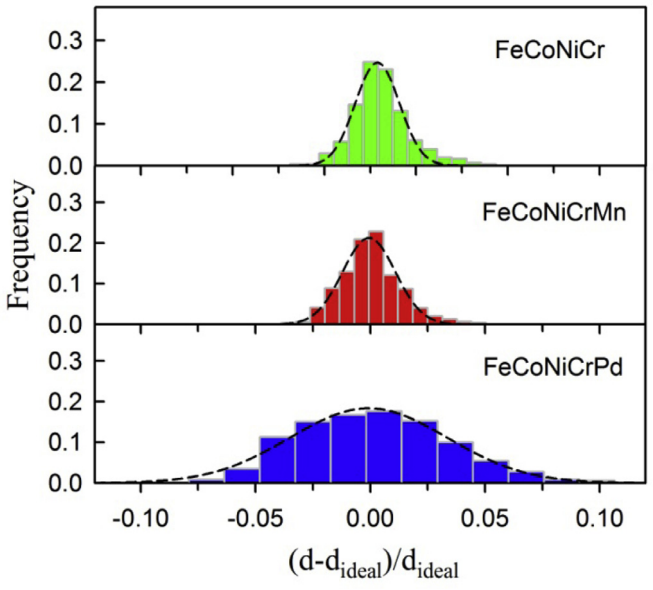

Fig. 9. DFT derived fluctuation of bond distances. Here, $d_{ideal} = a/\sqrt{2}$ where a is the lattice constant obtained from DFT calculations.

ducing local distortion into the ideal fcc structure through structure optimization in DFT calculations. Then, the distorted fcc supercell was fitted to the experimental data. Especially for the Pd-HEA, the quality of the fit is effectively improved compared with the ideal fcc structure (Fig. 7). The R_w is reduced from 0.119 to 0.086; meanwhile, the first peak is fitted accurately. The lattice constants are almost identical for the non-distorted and distorted fcc structure models. Notice that chemical homogeneity can also influence the local distortion. Here, we examined the chemical homogeneity of Pd-HEA by APT. The elemental distribution in Pd-HEA is shown in Fig. 8(a). A detailed concentration profile in Fig. 8(b) exhibits a random distribution of each component at atomic level. Therefore, the present PDF fitting based on the distorted supercell demonstrates that the local structure deviation is from the local lattice distortion.

Fig. 9 shows the fluctuation of bond distances derived from the DFT calculations. FeCoNiCr and Mn-HEA have a relatively narrow distribution of the bond distances while the bond fluctuation in Pd-HEA is twice the distribution of these two alloys. The highest change of bond distance in Pd-HEA can reach to 8%, which is slightly less than ~10% found in the bcc refractory HEAs [21]. The distributions in Fig. 9 are further analyzed by a Gaussian function, $f(x) = a * exp^{-\frac{1}{2}(\frac{x-\mu}{\sigma})^2}$, where μ and σ are the mean value and standard deviation, respectively. Here, the values of μ are too small to be accurately determined by DFT calculations (comparable with error). Table 2 shows that the value of σ qualitatively agrees with the predictions calculated from the hard-sphere model. Therefore, the calculated δ and ε_{RMS} based on the hard-sphere model resemble the fluctuations of local lattice distortions (i.e. σ), whereas the ε_{1st} obtained from the PDF measurements is the mean local lattice distortion. The departure of the DFT-derived σ from the δ and ε_{RMS} parameters may originate from the fixed atomic size in the hard-sphere model. Atomic size adopted in their calculations is empirically determined from some alloys or compounds, but average atomic size of an element varies from one composition to another, e.g., DFT calculations show that due to charge transfer Co atoms in FeCoNi MEA are under compressive strain while they are under tensile strain in FeCoNiCr MEA [55].

We further examined the contribution of each element to the overall fluctuation of bond distances in the three CSAs. Fig. 10 reveals that the Ni-Ni, Co-Co and Fe-Fe pairs in the FeCoNiCr MEA have a relatively narrow distribution of bond length changes while the Cr–Cr pairs show a flat distribution. In Mn-HEA, the Ni-Ni, Co–Co, Fe–Fe and Cr–Cr pairs show distributions similar to the FeCoNiCr MEA case; meanwhile, the Mn–Mn pairs exhibit a broad distribution, comparable with the Cr–Cr pairs. These findings are consistent with the recent first principle calculation results that the fluctuations of atomic displacements in the FeCoNiCr MEA and Mn-HEA follows the order of Cr > Mn > Fe > Co > Ni [53]. In Pd-HEA, the alloying of Pd strongly increases the fluctuation of the bond distances of the Ni-Ni, Co–Co, Fe–Fe and Cr–Cr pairs, but the Pd–Pd pairs exhibits a dramatically different distribution. The Pd–Pd pairs show a narrow distribution, suggesting a relatively well-defined Pd–Pd bond distance. Unlike other pairs, the distribution of the Pd–Pd pairs shifts from zero to the positive side, compatible with the observed shift of the first PDF peak (Fig. 2(b)). Therefore, the strong mean local lattice distortion found in Pd-HEA is attributed to the large bond distance of the Pd–Pd pairs (Fig. 10), i.e. large size mismatch between Pd and other four elements. Although the Pd atom has a larger size than the Ni, Co, Fe and Cr atoms, the large fluctuation of bond distances in these CSAs is resulted from the Cr atom and/or the Mn atom. Admittedly, large size mismatch can enhance the fluctuation of atomic displacements, but the general trend of the broad distribution for the Cr–Cr pair is not a simply size effect. Instead, after comparing the non-spin polarized DFT calculation with the DFT calculation counting magnetism,

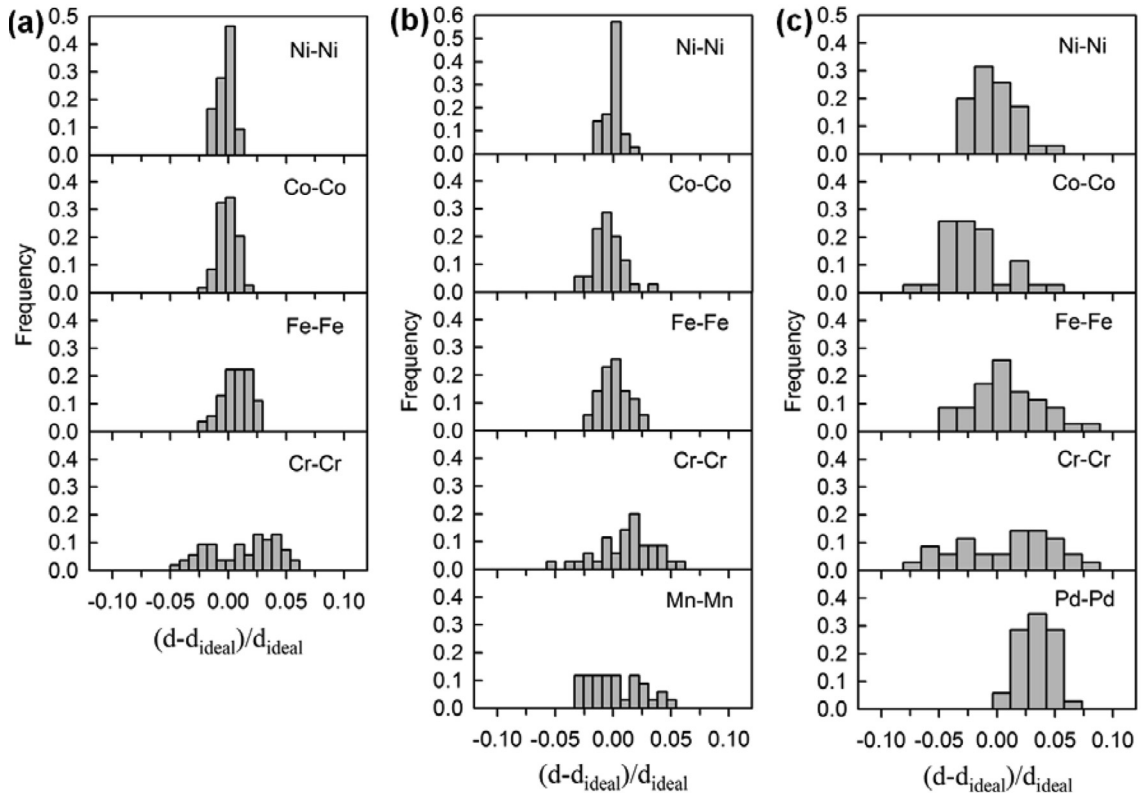

Fig. 10. DFT derived fluctuation of bond distances for A-A type atomic pairs in FeCoNiCr (a), Mn-HEA (b) and Pd-HEA (c).

Oh et al. [22] found that the large fluctuation in Mn-HEA is due to the magnetic frustration, i.e., Cr and Mn atoms prefer an antiferromagnetic alignment with the neighboring Fe, Co and Ni atoms [54].

The above discussions unveil that the mean local lattice distortion and the fluctuation of bond distances in Pd-HEA have distinct origins. Correspondingly, their interactions with dislocations should behave differently. Since the mean local lattice distortion is exclusively caused by strong size mismatch between Pd and other four elements, the classical solution strengthening model (i.e. Fleischer-type strong pinning [44]) is more suitable to estimate the strengthening, as illustrated in the 3.2 Section. However, solution strengthening in HEAs can also be influenced by the fluctuation of bond distances or atomic displacements. Varvenne et al. [56] proposed another solution strengthening model by approximating the HEA matrix as an effective distorted medium. Okamoto et al. [53] further demonstrated that the effective medium can be quantitatively described by the root mean square (RMS) of atomic displacements (equivalent to the standard deviation of the bond distance fluctuation, σ) and found a linear correlation between the yield strength of CSAs and their RMS values, $\sigma_Y/G \propto$ RMS, where G is shear modulus. This linear strengthening is not as strong as the Fleischer-type strengthening with a power-law relationship. Wu et al. [57] further experimentally confirmed that solute strengthening of the effective medium in fcc FeCoNiCr MEA and Mn-HEA is correlated with Labusch-type weak pinning. Thus, the strong mean local lattice distortion plays a key role in the delayed dislocation growth in the irradiated Pd-HEA.

5. Conclusions

To summarize, we have systemically investigated the evolution of local lattice distortion in FeCoNiCr, Mn-HEA and Pd-HEA before and after irradiation. Large atomic size misfit induces a strong mean local lattice distortion in Pd-HEA, which is further enhanced under ion irradiation. TEM results show a delay on the dislocation loop growth in Pd-HEA, suggesting the loops in Pd-HEA are at an early stage of loop evolution. We also revealed that, when HEAs are under irradiation at low dose, the local lattice distortion can be relaxed by lattice expansion. The present study provides new insights into radiation damage control by tuning the local lattice distortion. DFT calculations further revealed that the strong local lattice distortion observed in the Pd-HEA is resulted from the large bond distance of the Pd-Pd pairs. On the other hand, the bond distance of the Cr–Cr pairs has the largest fluctuation in the three studied CSAs, which can be further increased by alloying the large atom Pd. In contrast, the Pd–Pd pairs have a narrow distribution of bond distances. Pd atoms provide the Fleischer-type strong pinning on dislocations, whereas the broad distribution of the Cr–Cr pairs offers the Labusch-type weak pinning effect.

Acknowledgments

This work was supported as part of the Energy Dissipation to Defect Evolution (EDDE), an Energy Frontier Research Center funded by the U.S. Department of Energy, Office of Science, Basic Energy of Sciences. The X-ray PDF measurements were conducted at the Cornell High Energy Synchrotron Source (CHESS) which is supported by the National Science Foundation and the National Institutes of Health/National Institute of General Medical Sciences under NSF award DMR-1332208. The microstructure characterization was conducted in the Michigan Center for Material Characterization of the University of Michigan.

Supplementary materials

Supplementary material associated with this article can be found, in the online version, at doi:10.1016/j.mtla.2018.06.008.

References

[1] J.W. Yeh, S.K. Chen, S.J. Lin, J.Y. Gan, T.S. Chin, T.T. Shun, C.H. Tsau, S.Y. Chang, Nanostructured high-entropy alloys with multiple principal elements: novel alloy design concepts and outcomes, Adv. Eng. Mater. 6 (2004) 299–303.

[2] J.-W. Yeh, Alloy design strategies and future trends in high-entropy alloys, JOM 65 (2013) 1759–1771.

[3] B. Gludovatz, A. Hohenwarter, D. Catoor, E.H. Chang, E.P. George, R.O. Ritchie, A fracture-resistant high-entropy alloy for cryogenic applications, Science 345 (2014) 1153–1158.

[4] B. Gludovatz, A. Hohenwarter, K.V.S. Thurston, H. Bei, Z. Wu, E.P. George, R.O. Ritchie, Exceptional damage-tolerance of a medium-entropy alloy CrCoNi at cryogenic temperatures, Nat. Commun 7 (2016) 10602.

[5] F. Granberg, K. Nordlund, M.W. Ullah, K. Jin, C. Lu, H. Bei, L.M. Wang, F. Djurabekova, W.J. Weber, Y. Zhang, Mechanism of radiation damage reduction in equiatomic multicomponent single phase alloys, Phys. Rev. Lett. 116 (2016) 135504.

[6] Y. Zhang, G.M. Stocks, K. Jin, C. Lu, H. Bei, B.C. Sales, L. Wang, L.K. Béland, R.E. Stoller, G.D. Samolyuk, M. Caro, A. Caro, W.J. Weber, Influence of chemical disorder on energy dissipation and defect evolution in concentrated solid solution alloys, Nat. Commun. 6 (2015) 8736.

[7] C. Lu, L. Niu, N. Chen, K. Jin, T. Yang, P. Xiu, Y. Zhang, F. Gao, H. Bei, S. Shi, M.-R. He, I.M. Robertson, W.J. Weber, L. Wang, Enhancing radiation tolerance by controlling defect mobility and migration pathways in multicomponent single-phase alloys, Nat. Commun. 7 (2016) 13564.

[8] M.-H. Tsai, J.-W. Yeh, High-entropy alloys: a critical review, Mater. Res. Lett. 2 (2014) 107–123.

[9] K. Jin, B.C. Sales, G.M. Stocks, G.D. Samolyuk, M. Daene, W.J. Weber, Y. Zhang, H. Bei, Tailoring the physical properties of Ni-based single-phase equiatomic alloys by modifying the chemical complexity, Sci. Rep. 6 (2016) 20159.

[10] K. Jin, C. Lu, L.M. Wang, J. Qu, W.J. Weber, Y. Zhang, H. Bei, Effects of compositional complexity on the ion-irradiation induced swelling and hardening in Ni-containing equiatomic alloys, Scripta Mater 119 (2016) 65–70.

[11] C. Lu, T. Yang, K. Jin, N. Gao, P. Xiu, Y. Zhang, F. Gao, H. Bei, W.J. Weber, K. Sun, Y. Dong, L. Wang, Radiation-induced segregation on defect clusters in single-phase concentrated solid-solution alloys, Acta Mater 127 (2017) 98–107.

[12] M.J. Hackett, J.T. Busby, M.K. Miller, G.S. Was, J. Nucl, Effects of oversized solutes on radiation-induced segregation in austenitic stainless steels, Mater 389 (2009) 265–278.

[13] T. Kato, H. Takahashi, M. Izumiya, Grain boundary segregation under electron irradiation in austenitic stainless steels modified with oversized elements, J. Nucl. Mater 189 (1992) 167–174.

[14] G.S. Was, J.P. Wharry, B. Frisbie, B.D. Wirth, D. Morgan, J.D. Tucker, T.R. Allen, Assessment of radiation-induced segregation mechanisms in austenitic and ferritic—martensitic alloys, J. Nucl. Mater 411 (2011) 41–50.

[15] T.R. Allen, J.T. Busby, G.S. Was, E.A. Kenik, On the mechanism of radiation-induced segregation in austenitic Fe–Cr–Ni alloys, J. Nucl. Mater 255 (1998) 44–58.

[16] E.A. Little, Void-swelling in irons and ferritic steels, J. Nucl. Mater 87 (1979) 11–24.

[17] Y. Zhang, S. Zhao, W.J. Weber, K. Nordlund, F. Granberg, F. Djurabekova, Atomic-level heterogeneity and defect dynamics in concentrated solid-solution alloys, Curr. Opin. Solid State Mater. Sci. 21 (2017) 221–237.

[18] W. Guo, W. Dmowski, J.-Y. Noh, P. Rack, P.K. Liaw, T. Egami, Local atomic structure of a high-entropy alloy: an x-ray and neutron scattering study, Metall. Mat. Trans. A 44 (2013) 1994–1997.

[19] Y. Zou, S. Maiti, W. Steurer, R. Spolenak, Size-dependent plasticity in an Nb25Mo25Ta25W25 refractory high-entropy alloy, Acta Mater 65 (2014) 85–97.

[20] L.R. Owen, E.J. Pickering, H.Y. Playford, H.J. Stone, M.G. Tucker, N.G. Jones, An assessment of the lattice strain in the CrMnFeCoNi high-entropy alloy, Acta Mater 122 (2017) 11–18.

[21] H. Song, F. Tian, Q.-M. Hu, L. Vitos, Y. Wang, J. Shen, N. Chen, Local lattice distortion in high-entropy alloys, Phys. Rev. Mater. 1 (2017) 023404.

[22] H. Oh, D. Ma, G. Leyson, B. Grabowski, E. Park, F. Körmann, D. Raabe, Lattice Distortions in the FeCoNiCrMn high entropy alloy studied by theory and experiment, Entropy 18 (2016) 321.

[23] B. Cantor, I.T.H. Chang, P. Knight, A.J.B. Vincent, Microstructural development in equiatomic multicomponent alloys, Mater. Sci. Eng. A 375–377 (2004) 213–218.

[24] F. Otto, A. Dlouhý, C. Somsen, H. Bei, G. Eggeler, E.P. George, The influences of temperature and microstructure on the tensile properties of a CoCrFeMnNi high-entropy alloy, Acta Mater 61 (2013) 5743–5755.

[25] K.Y. Tsai, M.H. Tsai, J.W. Yeh, Sluggish diffusion in Co–Cr–Fe–Mn–Ni high-entropy alloys, Acta Mater 61 (2013) 4887–4897.

[26] Y. Zhang, M.L. Crespillo, H. Xue, K. Jin, C.H. Chen, C.L. Fontana, J.T. Graham, W.J. Weber, New ion beam materials laboratory for materials modification and irradiation effects research, Nucl. Instrum. Methods Phys. Res. B 338 (2014) 19–30.

[27] F.X. Zhang, S. Zhao, K. Jin, H. Xue, G. Velisa, H. Bei, R. Huang, J.Y.P. Ko, D.C. Pagan, J.C. Neuefeind, W.J. Weber, Y. Zhang, Local structure and short-range order in a NiCoCr solid solution alloy, Phys. Rev. Lett. 118 (2017) 205501.

[28] J.F. Ziegler, J.P. Biersack, U. Littmark, The Stopping and Range of Ions in Solids, Pergamon, 1985.

[29] A.P. Hammersley, S.O. Svensson, A. Thompson, Calibration and correction of spatial distortions in 2D detector systems, Nucl. Instrum. Methods Phys. Res. A 346 (1994) 312–321.

[30] P. Juhás, T. Davis, C.L. Farrow, S.J. Billinge, PDFgetX3: a rapid and highly automatable program for processing powder diffraction data into total scattering pair distribution functions, J. Appl. Cryst. 46 (2013) 560–566.

[31] C.L. Farrow, P. Juhas, J.W. Liu, D. Bryndin, E.S. Božin, J. Bloch, P. Th, S.J.L. Billinge, PDFfit2 and PDFgui: computer programs for studying nanostructure in crystals, J. Phys. Condens. Matter 19 (2007) 335219.

[32] T.-n. Yang, C. Lu, K. Jin, M.L. Crespillo, Y. Zhang, H. Bei, L. Wang, The effect of injected interstitials on void formation in self-ion irradiated nickel containing concentrated solid solution alloys, J. Nucl. Mater. 488 (2017) 328–337.

[33] G. Kresse, J. Furthmüller, Efficiency of ab-initio total energy calculations for metals and semiconductors using a plane-wave basis set, Comput. Mater. Sci. 6 (1996) 15–50.

[34] J.P. Perdew, K. Burke, M. Ernzerhof, Generalized Gradient approximation made simple, Phys. Rev. Lett. 77 (1996) 3865–3868.

[35] P.E. Blöchl, Projector augmented-wave method, Phys. Rev. B 50 (1994) 17953–17979.

[36] A. Zunger, S.H. Wei, L.G. Ferreira, J.E. Bernard, Special quasirandom structures, Phys. Rev. Lett. 65 (1990) 353–356.

[37] S. Zhao, G.M. Stocks, Y. Zhang, Stacking fault energies of face-centered cubic concentrated solid solution alloys, Acta Mater 134 (2017) 334–345.

[38] T. Egami, S.J.L. Billinge, Underneath the Bragg peaks: structural analysis of complex materials, Elsevier Sci. (2012).

[39] Z. Wu, H. Bei, G.M. Pharr, E.P. George, Temperature dependence of the mechanical properties of equiatomic solid solution alloys with face-centered cubic crystal structures, Acta Mater. 81 (2014) 428–441.

[40] S. Moll, L. Thomé, G. Sattonnay, A. Debelle, F. Garrido, L. Vincent, J. Jagielski, Multistep damage evolution process in cubic zirconia irradiated with MeV ions, J. Appl. Phys. 106 (2009) 073509.

[41] A. Debelle, A. Boulle, F. Rakotovao, J. Moeyaert, C. Bachelet, F. Garrido, L. Thomé, Influence of elastic properties on the strain induced by ion irradiation in crystalline materials, J. Phys. D Appl. Phys 46 (2013) 045309.

[42] M.W. Ullah, Y. Zhang, N. Sellami, A. Debelle, H. Bei, W.J. Weber, Evolution of irradiation-induced strain in an equiatomic NiFe alloy, Scr. Mater. 140 (2017) 35–39.

[43] G.S. Was, Fundamentals of Radiation Materials Science: Metals and Alloys, Springer, 2007, p. 313.

[44] R.L. Fleischer, Substitutional solution hardening, Acta Metal. 11 (1963) 203–209.

[45] M. Krčmar, C.L. Fu, A. Janotti, R.C. Reed, Diffusion rates of 3d transition metal solutes in nickel by first-principles calculations, Acta Mater 53 (2005) 2369–2376.

[46] A. Janotti, M. Krčmar, C.L. Fu, R.C. Reed, Solute diffusion in metals: larger atoms can move faster, Phys. Rev. Lett. 92 (2004) 085901.

[47] R. Ishikawa, R. Mishra, A.R. Lupini, S.D. Findlay, T. Taniguchi, S.T. Pantelides, S.J. Pennycook, Direct observation of dopant atom diffusion in a bulk semiconductor crystal enhanced by a large size mismatch, Phys. Rev. Lett. 113 (2014) 155501.

[48] S. Huang, D.L. Worthington, M. Asta, V. Ozolins, G. Ghosh, P.K. Liaw, Calculation of impurity diffusivities in α-Fe using first-principles methods, Acta Mater 58 (2010) 1982–1993.

[49] Y. Zhang, Y.J. Zhou, J.P. Lin, G.L. Chen, P.K. Liaw, Solid-solution phase formation rules for multi-component alloys, Adv. Eng. Mater. 10 (2008) 534–538.

[50] Y.F. Ye, C.T. Liu, Y. Yang, A geometric model for intrinsic residual strain and phase stability in high entropy alloys, Acta Mater 94 (2015) 152–161.

[51] Z. Wang, W. Qiu, Y. Yang, C.T. Liu, Atomic-size and lattice-distortion effects in newly developed high-entropy alloys with multiple principal elements, Intermetallics 64 (2015) 63–69.

[52] Y.F. Ye, Q. Wang, J. Lu, C.T. Liu, Y. Yang, High-entropy alloy: challenges and prospects, Mater. Today 19 (2016) 349–362.

[53] N.L. Okamoto, K. Yuge, K. Tanaka, H. Inui, E.P. George, Atomic displacement in the CrMnFeCoNi high-entropy alloy – a scaling factor to predict solid solution strengthening, AIP Adv. 6 (2016) 125008.

[54] Z. Wu, M.C. Troparevsky, Y.F. Gao, J.R. Morris, G.M. Stocks, H. Bei, Phase stability, physical properties and strengthening mechanisms of concentrated solid solution alloys, Curr. Opin. Solid State Mater. Sci. 21 (2017) 267–284.

[55] T. Egami, M. Ojha, O. Khorgolkhuu, D.M. Nicholson, G.M. Stocks, Local electronic effects and irradiation resistance in high-entropy alloys, JOM 67 (2015) 2345–2349.

[56] C. Varvenne, A. Luque, W.A. Curtin, Theory of strengthening in fcc high entropy alloys, Acta Mater 118 (2016) 164–176.

[57] Z. Wu, Y. Gao, H. Bei, Thermal activation mechanisms and Labusch-type strengthening analysis for a family of high-entropy and equiatomic solid-solution alloys, Acta Mater 120 (2016) 108–119.